Biochemistry **2000,** *39,* 2499−2508

Structures of the Superoxide Reductase from *Pyrococcus furiosus* in the Oxidized and Reduced States[†,‡]

Andrew P. Yeh,[§] Yonglin Hu,[§,||] Francis E. Jenney, Jr.,[⊥] Michael W. W. Adams,[⊥] and Douglas C. Rees*[,§,@]

Division of Chemistry and Chemical Engineering, 147-75CH, California Institute of Technology, Pasadena, California 91125,
Department of Biochemistry and Molecular Biology, University of Georgia, Athens, Georgia 30602, and
Howard Hughes Medical Institute, California Institute of Technology, Pasadena, California 91125

Received October 19, 1999; Revised Manuscript Received December 22, 1999

ABSTRACT: Superoxide reductase (SOR) is a blue non-heme iron protein that functions in anaerobic microbes as a defense mechanism against reactive oxygen species by catalyzing the reduction of superoxide to hydrogen peroxide [Jenney, F. E., Jr., Verhagen, M. F. J. M., Cui, X., and Adams, M. W. W. (1999) *Science 286*, 306−309]. Crystal structures of SOR from the hyperthermophilic archaeon *Pyrococcus furiosus* have been determined in the oxidized and reduced forms to resolutions of 1.7 and 2.0 Å, respectively. SOR forms a homotetramer, with each subunit adopting an immunoglobulin-like β-barrel fold that coordinates a mononuclear, non-heme iron center. The protein fold and metal center are similar to those observed previously for the homologous protein desulfoferrodoxin from *Desulfovibrio desulfuricans* [Coelho, A. V., Matias, P., Fülöp, V., Thompson, A., Gonzalez, A., and Carrondo, M. A. (1997) *J. Bioinorg. Chem. 2*, 680−689]. Each iron is coordinated to imidazole nitrogens of four histidines in a planar arrangement, with a cysteine ligand occupying an axial position normal to this plane. In two of the subunits of the oxidized structure, a glutamate carboxylate serves as the sixth ligand to form an overall six-coordinate, octahedral coordinate environment. In the remaining two subunits, the sixth coordination site is either vacant or occupied by solvent molecules. The iron centers in all four subunits of the reduced structure exhibit pentacoordination. The structures of the oxidized and reduced forms of SOR suggest a mechanism by which superoxide accessibility may be controlled and define a possible binding site for rubredoxin, the likely physiological electron donor to SOR.

Superoxide reductases (SORs)[1] are mononuclear, non-heme iron proteins that catalyze the one-electron reduction of superoxide to peroxide (*1*):

$$\mathrm{SOR{\cdot}Fe^{2+} + O_2^{-} + 2H^{+} \rightarrow SOR{\cdot}Fe^{3+} + H_2O_2} \quad (1a)$$

$$\mathrm{D_{red} + SOR{\cdot}Fe^{3+} \rightarrow D_{ox} + SOR{\cdot}Fe^{2+}} \quad (1b)$$

The electron donor for reduction reaction 1b is likely a second non-heme iron protein, rubredoxin, which is reduced by an oxidoreductase using NAD(P)H (*1*). SORs are distinct from superoxide dismutases (SODs) since SORs do not couple the reduction of one superoxide molecule to the oxidation of a second superoxide to yield dioxygen. It has recently been proposed (*1*) that SORs participate in a novel oxygen detoxification system that is utilized by all anaerobic microorganisms that cannot tolerate the production of dioxygen generated from superoxide by the action of SOD.

The SOR from the hyperthermophilic archaeon *Pyrococcus furiosus* is the most extensively characterized member of this family (*1*); it is organized as a homotetramer composed of 14.3 kDa subunits each containing a single mononuclear non-heme iron. The oxidized enzyme exhibits a characteristic blue color that prompted the name neelaredoxin (derived from *neela*, the Sanskrit word for blue) originally assigned to a homologous protein (50% identical to the *P. furiosus* protein) of undetermined function isolated from *Desulfovibrio gigas* (*2*). SOR also shares extensive sequence similarity (40% identity) with the 93-residue C-terminal domain of *Desulfovibrio desulfuricans* desulfoferrodoxin (DFX), which is an electron-transfer protein of unassigned function (*3*). A

[†] This work was supported in part by grants from the Department of Energy (FG05-95ER20175) and the National Science Foundation (MCB 9809060) to M.W.W.A. and from the National Institutes of Health (GM45162) to D.C.R. A.P.Y. was supported in part by a National Science Foundation Graduate Research Fellowship. The protein crystallographic facility at the Stanford Synchrotron Radiation Laboratory (SSRL) is funded by the Department of Energy, Office of Basic Energy Sciences, the National Institutes of Health, National Center for Research Resources, Biomedical Technology Program, and the Department of Energy, Office of Biological and Environmental Research.

[‡] Coordinates have been deposited in the RCSB Protein Data Bank, entries 1DO6, 1DQI, and 1DQK.

* To whom correspondence should be addressed. Telephone: (626) 395-8393. Fax: (626) 744-9524. E-mail: dcrees@caltech.edu.

[§] California Institute of Technology.

[||] Present address: Department of Physiology and Microbiology and Molecular Genetics, Howard Hughes Medical Institute, University of California at Los Angeles, Los Angeles, CA 90095.

[⊥] University of Georgia.

[@] Howard Hughes Medical Institute, California Institute of Technology.

[1] Abbreviations: SOR, superoxide reductase; SOR-OxRT, superoxide reductase in the oxidized form at room temperature; SOR-OxLT, superoxide reductase in the oxidized form at low temperature; SOR-RedLT, superoxide reductase in the reduced form at low temperature; DFX, desulfoferrodoxin; Rd, rubredoxin; SOD, superoxide dismutase.

10.1021/bi992428k CCC: $19.00

Table 1: Data Sets and Heavy Atom Phasing Statistics[a]

	SOR-OxRT[b]	SOR-OxLT	SOR-RedLT	TMLA	$Pt(NH_3)_2Cl_2$	$HgCl_2$	Xe
source	CuKα	SSRL BL9−1	CuKα	CuKα	CuKα	CuKα	CuKα
wavelength	1.54	0.98	1.54	1.54	1.54	1.54	1.54
temperature	room temp	90 K	90 K	room temp	room temp	room temp	room temp
space group	$P2_12_12$	$P2_12_12_1$	$P2_12_12_1$	$P2_12_12$	$P2_12_12$	$P2_12_12$	$P2_12_12$
unit cell dimensions (Å)							
a	50.31	49.54	49.84	50.25	50.58	50.10	49.94
b	94.02	93.01	93.21	93.78	93.85	93.93	93.46
c	52.90	99.32	99.97	52.49	52.63	52.68	52.66
maximum resolution (Å)	2.0	1.7	2.0	2.5	3.0	2.8	3.0
no. of measurements	65376	222107	92775	24656	21012	23723	17184
no. of unique reflections	16334	51080	31825	8285	5358	6483	5243
completeness (%)[c]	92.9 (84.2)	99.5 (99.8)	98.7 (95.7)	91.5 (79.9)	99.8 (98.4)	99.6 (97.0)	98.7 (96.8)
$I/\sigma(I)$	23.8 (4.4)	21.7 (5.5)	19.2 (4.7)	15.0 (6.8)	15.1 (8.3)	13.4 (4.8)	17.8 (8.3)
R_{sym} (%)[d]	6.2 (17.8)	6.3 (25.1)	6.0 (24.2)	7.9 (11.7)	8.7 (13.8)	10.1 (19.2)	6.5 (14.0)
concentration of heavy-atom compound (mM)	−	−	−	10	2	2	∼15 atm.
no. of sites	2	−	−	2	3	3	1
phasing power[e]	−	−	−	1.04	0.72	0.96	0.86
R_{cullis}[f]	0.85	−	−	0.83	0.89	0.85	0.88
overall FOM				0.515 (to 3.0 Å resolution)			

[a] The native anomalous signal and TMLA and $Pt(NH_3)_2Cl_2$ derivatives were phased to 3.0 Å; the $HgCl_2$ derivative was phased to 3.5 Å, while the xenon derivative was phased to 4.0 Å. [b] The room-temperature oxidized SOR data set was used for the initial MIR phasing. [c] Numbers in parentheses correspond to values in the highest-resolution shell. [d] $R_{sym} = [\Sigma_{hkl}\Sigma_i|I_i(hkl) - \langle I(hkl)\rangle|]/[\Sigma_{hkl}\Sigma_i I(hkl)]$. [e] Phasing power $= \langle F_H\rangle/\Sigma||F_{PH} - F_P| - F_H|$, where $\langle F_H\rangle$ is the rms calculated heavy atom structure factor. [f] $R_{cullis} = \Sigma||F_{PH} - F_P| - F_H|/\Sigma|F_{PH} - F_P|$, where F_H is the calculated heavy atom structure factor amplitude and F_P and F_{PH} are the native and derivative structure factor amplitudes, respectively.

recent crystal structure analysis of DFX (*4*) demonstrated that this domain binds Fe in a square planar coordination geometry generated by four histidine rings in a plane, with a fifth ligand, cysteine, occupying an axial position.

In view of the biochemical and spectroscopic characterization of the SOR which established the SOR activity of this center, and the available structural analyses of the likely physiological electron donor to this center, *P. furiosus* rubredoxin (*5*, *6*), we have determined the crystal structures of the *P. furiosus* SOR in the oxidized state (room temperature and low temperature to resolutions of 2.0 and 1.7 Å, respectively) and in the reduced state at low temperature to 2.0 Å resolution, to provide a structural framework for the interpretation of the spectroscopic properties and mechanistic features of this protein.

MATERIALS AND METHODS

Crystallization and Data Collection. SOR was overexpressed and purified as described in ref *7*. Crystals of SOR for data collection were prepared by the sitting drop vapor diffusion method, following a PEG screen, using 2 μL of ∼100 mg/mL SOR in 50 mM Tris-HCl buffer at pH 8.0 and 2 μL of reservoir solution equilibrated against a reservoir solution containing 22% PEG 4000, 100 mM Tris-HCl at pH 8.0, 10% (v/v) glycerol, 200 mM NaCl, and 2% (v/v) ethanol. Crystals appeared within 4−5 days after setup and belong to orthorhombic space group $P2_12_12$ ($a = 50.31$ Å, $b = 94.02$ Å, and $c = 52.90$ Å), with two SOR subunits in the asymmetric unit (solvent content of ∼44%).

Three native data sets were collected from SOR crystals. (a) For SOR-OxRT, diffraction data to 2.0 Å resolution were collected from a capillary-mounted, oxidized crystal at room temperature on a Siemens multiwire area detector using monochromatized CuKα radiation produced by a Siemens rotating anode generator operated at 50 kV and 90 mA. The data set was processed and scaled using the XDS package (*8*). (b) For SOR-OxLT, after soaking in a mother liquor solution containing 20% (v/v) PEG 400, SOR crystals could be flash-cooled. This development permitted collection of a second oxidized native data set at ∼90 K to 1.7 Å resolution on beamline 9-1 at the Stanford Synchrotron Radiation Laboratory ($\lambda = 0.98$ Å) on a 34.5 cm MAR Research imaging plate system. The data set was processed and scaled using DENZO and SCALEPACK (*9*). Upon flash-cooling the crystal, the unit cell dimension along the *c* axis nearly doubled in length, increasing from 52.90 to 99.33 Å, and the space group changed from $P2_12_12$ to $P2_12_12_1$ (Table 1). This change in the space group resulted from a slight shift in the crystal packing upon flash-cooling, causing the crystallographic 2-fold axis to become noncrystallographic. (c) For SOR-RedLT, SOR crystals were reduced by placing a few grains of sodium dithionite in the crystal-containing drop and were deemed fully reduced when the crystals became colorless. A 2.0 Å resolution data set of SOR in its reduced form was collected under cryogenic temperatures on an R-Axis IV imaging plate area detector using monochromatized CuKα radiation produced by a Rigaku RU 200 rotating anode generator operated at 50 kV and 100 mA. The data set was processed and scaled using DENZO and SCALEPACK (*9*).

Heavy Atom Derivatives and Phasing. Heavy atom derivatives for the SOR-OxRT crystal form were prepared by soaking SOR crystal(s) in mother liquor solutions containing either 10 mM trimethyllead acetate (TMLA), 2 mM $Pt(NH_3)_2Cl_2$, or 2 mM $HgCl_2$. In addition to those three heavy atom compounds, xenon gas was used for heavy atom derivatization. Derivatization with xenon gas was carried out by mounting an SOR crystal in a quartz capillary and applying ∼15 atm of xenon gas to the capillary approximately 30 min before and throughout data collection (*10*). All heavy atom derivative data sets were collected at room temperature on an R-Axis IIC imaging plate area

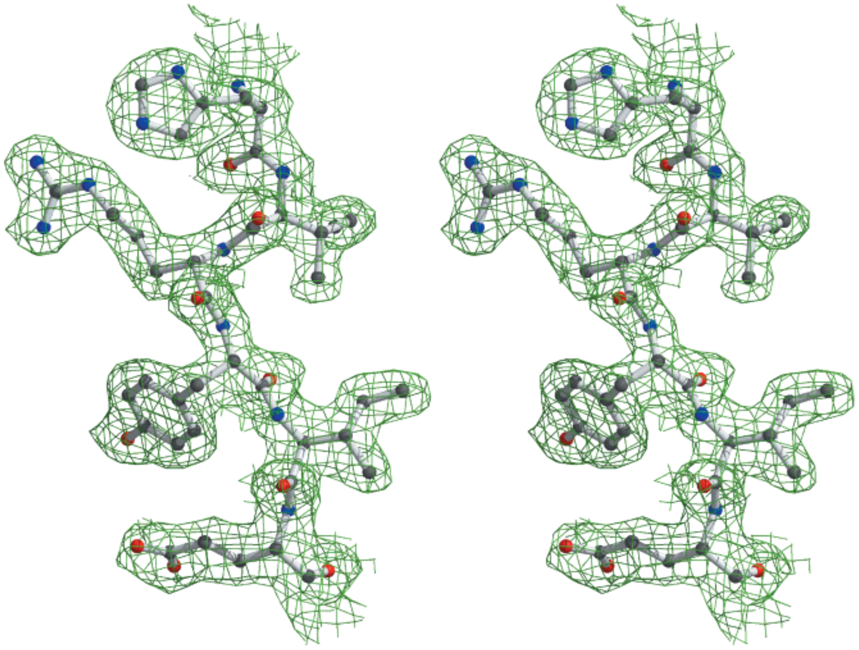

FIGURE 1: Stereoview of the final σA-weighted $2|F_o| - |F_c|$ electron density map around residues 48−53 of the SOR-OxRT structure. The map was calculated to 2.0 Å resolution and contoured at 1.0σ. This and all subsequent figures, unless indicated otherwise, were produced using the programs BOBSCRIPT (*28*) and RASTER3D (*29*).

detector using monochromatized CuKα radiation produced by a Rigaku RU 200 rotating anode generator operating at 50 kV and 100 mA and processed using the programs DENZO and SCALEPACK (*9*). Heavy atom sites, including the native Fe sites, were identified by a combination of anomalous Patterson, difference Patterson, and cross-difference Fourier maps generated with the CCP4 suite of programs (*11*). A total of nine heavy atom sites [two TMLA sites, three $Pt(NH_3)_2Cl_2$ sites, three $HgCl_2$ sites, and one xenon site] were found. These sites, in combination with the two native iron sites, were used to calculate phases to 3.0 Å resolution using MLPHARE (*12*). A summary of the statistics for all data sets and phasing is listed in Table 1.

Model Building and Refinement. The initial MIR electron density map for the SOR-OxRT structure was improved through the use of 2-fold noncrystallographic symmetry (NCS) averaging and solvent flattening using the program DM (*13*). An approximate Cα trace of the model was built using the program XDLMAPMAN (*14*) and was used as a starting point for model building. Initial refinement employed strict NCS constraints in the simulated annealing protocol of the program X-PLOR (*15*), using a bulk solvent correction and all data between ∼30 and 2.0 Å resolution. Refinement cycles were alternated with model rebuilding against $2|F_o| - |F_c|$ σ_A-weighted and $|F_o| - |F_c|$ σ_A-weighted maps (*16*) using the molecular graphics program O (*17*). After several rounds of refinement and model rebuilding, the *R*-factor and *R*-free converged to 16.0 and 18.9%, respectively. The final SOR-OxRT model contains two subunits (2 × 124 amino acid residues), two iron atoms, and 128 water molecules. The overall structures of the two NCS-related subunits are very similar, with the exception of the regions spanning Gly 9−Lys 15 and Gly 36−Pro 40. Of the 128 water molecules, 56 are NCS-related while 72 are not. A representative segment of the final σ_A-weighted $2|F_o| - |F_c|$ electron density map calculated at 2.0 Å resolution is shown in Figure 1. The final model displays good stereochemistry, with an rms deviations in bond lengths and bond angles of 0.010 Å and 1.49°, respectively. The average temperature factors of subunits A and B are 25.0 and 27.9 Å^2, respectively, while the average temperature factor for the 128 water molecules is 34.3 Å^2. In the Ramachandran plot, as calculated with PROCHECK (*18*), 92.9% of the residues are in the most favored regions while 7.1% of the residues are in additionally allowed regions. There are no residues in disallowed regions.

Since the space group of the crystals changed from $P2_12_12$ to $P2_12_12_1$ upon flash-cooling, the SOR-OxLT structure was determined by molecular replacement using the molecular replacement package AMoRe (*19*). Successive rounds of refinement and model rebuilding resulted in the convergence of the *R*-factor and *R*-free to 20.3 and 21.7%, respectively. The final SOR-OxLT model contains four subunits (4 × 124 amino acid residues), four iron atoms, and 416 water molecules. As was the case for the SOR-OxRT model, the overall structures of the four subunits in the low-temperature oxidized SOR model are very similar, except for the regions spanning Gly 9−Lys 15 and Lys 37−Pro 40. The average *B*-factors for subunits A−D are 17.1, 18.7, 16.6, and 18.9 Å^2, respectively. The rms deviations in bond lengths and bond angles of SOR-OxLT are 0.004 Å and 1.24°, respectively. Further analysis with PROCHECK (*18*) showed that 94.9% of the residues reside in the most favored regions while 5.1% of the residues reside in the additionally allowed regions of the Ramachandran plot.

The SOR-OxLT structure, excluding the iron atoms and water molecules, was used as the starting model for the refinement of the SOR-RedLT structure. Successive rounds of simulated annealing, positional, and individual *B*-factor refinement in X-PLOR (*15*) using all data between 30 and 2.0 Å resolution were alternated with model rebuilding. The occupancies of Lys 12, Gly 13, Glu 14, and Lys 15 were set to 0.10 due to the absence of electron density for those

Table 2: Final Refinement Statistics for the SOR Models in the Oxidized (SOR-OxRT and SOR-OxLT) and Reduced (SOR-RedLT) Forms

	SOR-OxRT	SOR-OxLT	SOR-RedLT
resolution limits (Å)	28.8−2.0	29.6−1.7	22.7−2.0
R-factor[a]	0.160	0.203	0.222
R-free	0.189	0.217	0.247
no. of monomers/asymmetric unit (au)	2	4	4
no. of non-hydrogen atoms/au			
no. of protein atoms	2028	4056	4056
no of iron atoms	2	4	4
no. of water atoms	128	416	330
rms deviations from ideal values			
bond lengths (Å)	0.010	0.004	0.006
bond angles (deg)	1.49	1.24	1.58
dihedral angles (deg)	29.9	29.6	29.3
improper torsion angles (deg)	0.73	0.55	0.68
average temperature factor (Å^2)			
main chain atoms	23.9	16.5	26.2
side chain atoms	28.9	19.1	28.1
water molecules	34.3	31.3	40.7
Ramachandran plot (%)			
residues in most favored regions	92.9	94.9	92.2
residues in additional allowed regions	7.1	5.1	7.8
residues in generously allowed regions	0.0	0.0	0.0
residues in disallowed regions	0.0	0.0	0.0

[a] *R*-factor = $\Sigma(|F_{\mathrm{obs}}| - |F_{\mathrm{calc}}|)/\Sigma|F_{\mathrm{obs}}|$.

residues. The iron atoms, which were initially left out of the model, were placed back into all four subunits upon observing $2|F_o| - |F_c|$, $|F_o| - |F_c|$, and anomalous difference electron density at the iron sites in all four subunits. However, the electron densities at the iron sites in subunits A and C were considerably stronger than those in subunits B and D, suggesting that the iron atoms in subunits B and D were either at lower occupancy or more disordered. To distinguish between the two situations, two different refinements were performed and the resulting maps were compared. In one case, the occupancies of the iron atoms in subunits B and D were held constant at 1.0 while their *B*-factors were refined, whereas in the other case, the *B*-factors of the two irons were fixed at their values in the SOR-OxLT model (∼27 Å^2) while their occupancies were refined. Comparison of the positive and negative difference density around the iron sites under each scenario suggested that the iron atoms in subunits B and D are present and ordered, but at low occupancy. The occupancies of the iron atoms in subunits B and D were ultimately refined to 0.22 and 0.24, respectively. Alternating rounds of refinement and rebuilding resulted in a final *R*-factor and a final *R*-free of 22.2 and 24.7%, respectively.

The final model of SOR in the reduced form at low temperature consists of four subunits (4 × 124 amino acid residues), four iron atoms, and 330 water molecules. The rms deviations from ideal bond lengths and bond angles are 0.006 Å and 1.58°, respectively, while in the Ramachandran plot, 92.2% of the residues are in the most favored regions and 7.8% of the residues are in additionally allowed regions. The average *B*-factors for each of the subunits (A−D) are 26.6, 27.6, 26.2, and 28.4 Å^2, respectively, and that for the water molecules is 40.7 Å^2. Refinement statistics for all structures are summarized in Table 2.

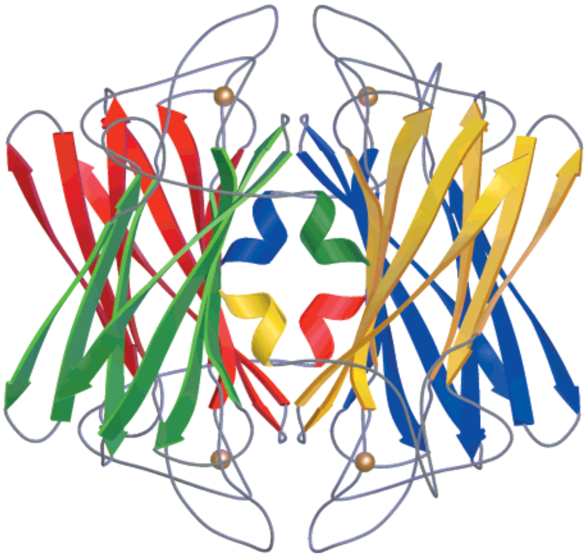

FIGURE 2: Ribbon diagram of the homotetrameric arrangement of SOR. Subunits A−D are depicted in yellow, green, blue, and red, respectively, while iron atoms are depicted as gold spheres.

RESULTS AND DISCUSSION

Structural Organization of SOR. SOR exists as a homotetramer with 222 point group symmetry in the crystal structure (Figure 2). The overall dimensions of the tetramer are approximately 45 Å × 49 Å × 53 Å. The SOR subunit is organized as a seven-stranded *β*-barrel that adopts an immunoglobulin-like fold, with one turn of 3_{10}-helix (residues 1−4) connected to the barrel by a 15-residue loop at the N-terminus (Figure 3A). As expected, this structure is similar to the fold observed for the C-terminal domain of desulfoferrodoxin (DFX), with an rmsd of 1.3 Å between 72 Cα atoms of SOR-OxLT and DFX (Figure 4). The topology of the seven *β*-strands corresponds to that of a C2-type Ig-like fold, which is characterized by the strand order A, B, E, D, C, F, and G (*20*) (Figure 3B). The three-stranded antiparallel *β*-sheet contains *β*-strands A (residues 19−25), B (residues 28−34), and E (residues 92−98), while the four-stranded *β*-sheet consists of *β*-strands C (residues 49−58), D (residues 65−71), F (residues 103−111), and G (residues 115−123). The main difference between SOR and the C-terminal domain of DFX is that the loop regions in SOR are longer. In SOR, loops A−B, C−D, D−E, and E−F are longer than they are in DFX by 4, 6, 13, and 3 residues, respectively (Figure 4).

In the SOR-OxRT model, subunits A and C are crystallographically equivalent, as are subunits B and D. Subunits A and B, related by noncrystallographic symmetry (as are subunits C and D), are nearly identical to each other, with two regions of notable exception (Figure 5A). One region spans Gly 9−Lys 15, while the other includes Gly 36−Pro 40. The difference between the two subunits in the Gly 9−Lys 15 region adjacent to the iron site is quite substantial (Figure 5B), with a rmsd of 6.4 Å between corresponding Cα atoms. The differences between the region spanning Gly 36−Pro 40 are less drastic, with a rmsd between corresponding Cα atoms of 1.2 Å. Excluding these two regions, the Cα rms fit between the remaining 113 residues in the two subunits is 0.1 Å. Similar relationships between these regions are observed in the SOR-OxLT structure.

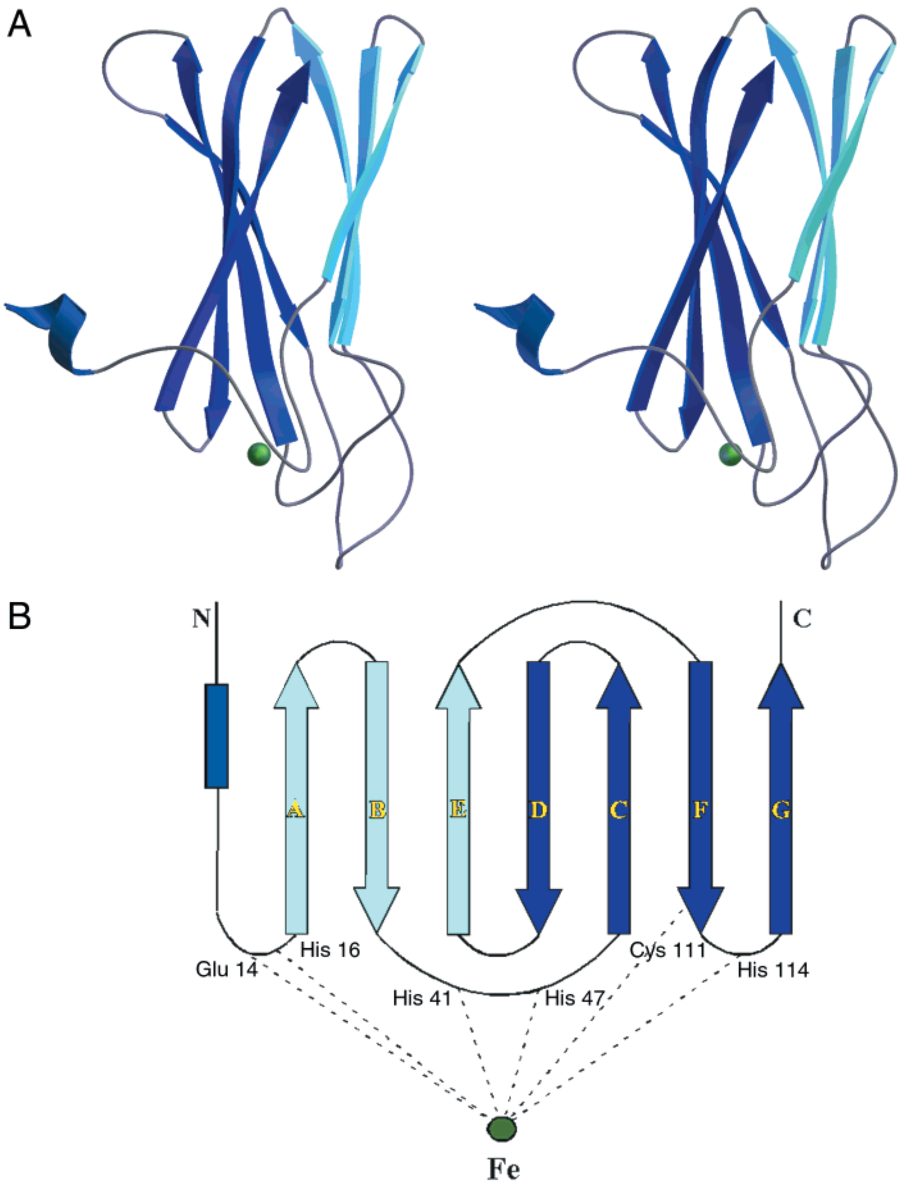

FIGURE 3: (A) Stereoview of the structure of a SOR monomer. β-Strands in the three-stranded and four-stranded β-sheets are shown in light and dark blue, respectively. The iron atom is depicted as a green sphere. (B) Topology diagram of a SOR monomer. Secondary structures are depicted using the same color scheme as in panel A. β-Strands are lettered A−G, with the order of the strands being such that the topology is that of a C2 Ig-like fold. β-Strands A, B, and E form the three-stranded β-sheet, while β-strands C, D, F, and G form the four-stranded β-sheet. The iron center is shown as a green sphere and is connected by dotted lines to the general locations of its five, potentially six, ligands.

Such drastic differences between the subunits in these two regions were not observed, however, in the SOR-RedLT structure. The average rmsds between the Cα atoms in the different subunits of the regions spanning Gly 9−Lys 15 and Gly 36−Pro 40 in this structure are only 0.3 and 0.5 Å, respectively, making all four subunits in the asymmetric unit nearly identical to one another.

Intersubunit Interactions. Each subunit forms extensive contacts with the other three subunits, resulting in the burial at subunit−subunit interfaces of ~40% of the surface area of each isolated subunit, as calculated with GRASP (*21*). Two of the NCS-related subunits in SOR-OxRT, A and B (which are equivalent to C and D, respectively), form a tight dimer that is held together by many hydrogen bonds and electrostatic interactions. The interface area between these two subunits, calculated using GRASP, was found to be ~1340 Å^2 per subunit. The numerous interactions that are formed involve residues from the 3_{10}-helix, the loop region connecting β-strands C and D, and β-strands C, D, F, and G. The two crystallographically related subunits (A and C) also interact extensively, with the surface area buried at this interface calculated to be ~1360 Å^2 per subunit. A notable feature of subunits A and C pair is that the four-stranded antiparallel β-sheets of the two subunits are juxtaposed such that β-strands D of subunits A and C pair up to form an extended eight-stranded antiparallel β-sheet (Figure 6A). A similar dimerization interaction between the four-stranded β-sheets is observed in desulfoferrodoxin (*4*). In addition, in SOR, residues 88−98 from β-strand E of subunit A form water-mediated as well as direct hydrogen bonds to the corresponding residues on β-strand E from subunit C (Figure 6B). The other NCS-related subunits, A and D (equivalent to C and B, respectively), also interact with each other, but to a much lesser extent than the first pair of NCS-related

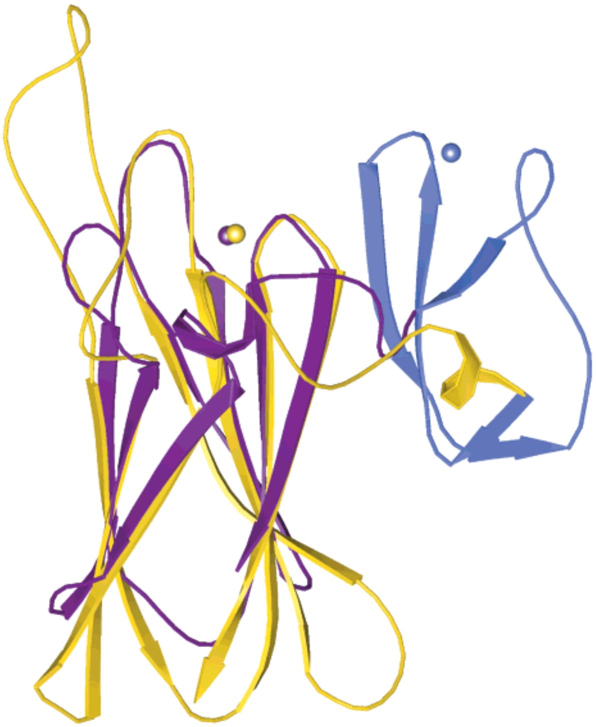

FIGURE 4: Superposition of SOR (yellow) and DFX domain II (darker purple) showing the similarity between the folds (rmsd among 72 Cα atoms of SOR-OxLT and the DFX domain II of 1.3 Å). Domain I of DFX, which contains a rubredoxin-like $FeCys_4$ center, is shown in light purple.

subunits. The calculated dimer interface for subunits A and D (~590 $Å^2$ per subunit) is less than half that of either of the other two NCS-related subunit pairs. Finally, it is interesting to note that at the core of the homotetramer, near where the three molecular 2-fold axes intersect, are located a number of buried charged residues. Arginine 69 and glutamates 53 and 71 from each of the subunits are positioned near the 2-fold axes such that they form direct and water-mediated hydrogen bonds as well as electrostatic interactions with one another.

Iron Center. Each SOR subunit in the homotetramer contains one mononuclear, non-heme iron center that resides on the periphery of the subunit between three loop regions: the loop region between the 3_{10}-helix and β-strand A, the loop region between β-strands B and C, and the loop region between β-strands F and G (Figure 3A). The coordination geometry in subunits A and C of the oxidized structures may be described as octahedral, with four histidine ligands (His 16, His 41, His 47, and His 114) arranged in an equatorial plane, and a cysteine ligand (Cys 111) and a glutamate ligand (Glu 14) positioned axially (Figure 7A). Three of the four histidines (His 16, His 41, and His 47) coordinate the iron via their Nϵ2 atoms, while the fourth histidine, His 114, coordinates the iron via its Nδ2 atom.

Differences are observed in the sixth coordination position in subunits B and D of oxidized SOR. In SOR-OxRT, where Glu 14 is the sixth ligand in subunits A and C (which are identical due to crystallographic symmetry), no ligand is present at this position in subunits B and D (which are also crystallographically related). This pentacoordination geometry, as shown in Figure 7B, is similar to that observed for the iron center seen in domain II of DFX (*4*).

The iron centers seen in SOR-OxLT are indistinguishable from those seen in SOR-OxRT in most respects except for one. Where a sixth iron ligand was not observed in subunits B and D in the SOR-OxRT model, electron density for a solvent molecule in that position is now observed ~2.6 Å from the iron. The distances between the iron center and its ligands for all three SOR structures are listed in Table 3.

The differences in metal coordination observed between the iron centers of subunits A and C, and B and D, in both oxidized SOR structures reflect the substantial differences, as discussed earlier, in the polypeptide conformation for residues Gly 9−Lys 15 (Figure 5B). In subunits B and D, this region is positioned such that Glu 14 is displaced from the iron center. The weak electron density, as well as the considerably higher temperature factors observed in this region of subunits B and D, indicates that it is probably somewhat disordered. As further evidence for the greater disorder of this region in subunits B and D than in subunits A and C, the refined temperature factor for the iron atoms in subunits B and D (26 $Å^2$) of the SOR-OxRT model is higher than that of the iron atoms in subunits A and C (17 $Å^2$). Whether the flexibility observed in this Gly 9−Lys 15 loop region is mechanistically relevant is unclear. It is interesting to note that the other loop region that differs between the subunits, Gly 36−Pro 40, is in close contact with the Gly 9−Lys 15 loop region. It seems plausible, therefore, that the interactions between these two regions of the subunit are correlated and could play a role in the catalytic mechanism of the enzyme.

The origin of the differences in the polypeptide conformations and the resulting differences in iron coordination between the different subunits of oxidized SOR is unclear. One possibility is that oxidized SOR may exist in an equilibrium between two different conformations and that the observed structures represent a trapped mixture of the two different oxidized conformations (with subunits A and C displaying one conformation and subunits B and D displaying the other). Yet another possibility is that the conformational differences observed in the oxidized structures arise from crystal packing. The molecules are packed in such a way that Trp 11 and Lys 12 of subunits A and C form lattice contacts with residues from an adjacent crystallographically related molecule, while the same residues in subunits B and D are not in contact with any residues from another molecule. It might be argued then that the crystal packing interactions present in subunits A and C could be the cause for the greater stability observed in the Gly 9−Lys 15 loop region of these subunits. However, analysis of the reduced structure indicates otherwise. As will be discussed subsequently, all four subunits in the reduced SOR structure adopt the same conformation in the flexible regions. The homogeneity of the subunits in the reduced structure suggests that crystal packing is unlikely to be the sole determinant of the conformation of the flexible regions. While crystal packing may still play a role, the reduced structure shows that the conformational differences observed in the oxidized structures are not necessarily enforced by crystal packing. A third possibility is that the iron sites of two of the subunits were photoreduced by X-rays during data collection, as has been previously observed for Cu,Zn SOD (*22*, *23*), and the resulting structures represent a mixture of oxidized and reduced states. Such a scenario appears to be

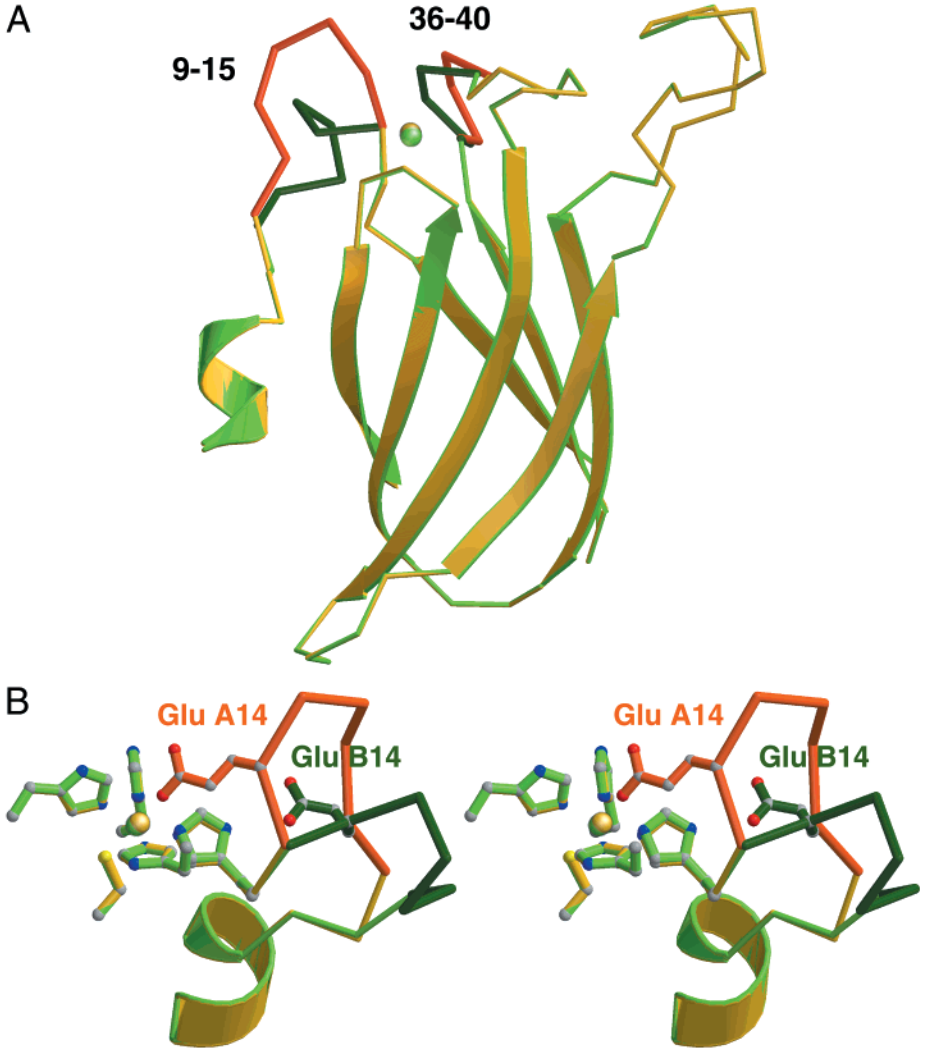

FIGURE 5: (A) Superposition of subunits A (yellow) and B (green) of SOR in the oxidized form. The two regions (Gly 9−Lys 15 and Gly 36−Pro 40) that differ between the subunits are shown in a darker shade of their respective colors. (B) Stereoview of the superposition of the iron centers of subunits A and B in oxidized SOR using the same color scheme as in panel A. Glu 14 is located on one of the flexible loop regions (shown in a darker shade) which differ in conformation between subunits A and B. One result of this conformational difference is that in subunit A, Glu 14 can act as a sixth ligand to the iron whereas in subunit B, Glu 14 has moved ∼5 Å away and, as a result, no longer can act as a sixth ligand.

more likely than either of the first two possibilities. The conformations of the flexible regions in subunits B and D of the oxidized structures are the same as that of the corresponding regions in all four subunits of the reduced structure, suggesting that subunits B and D in the oxidized structures might actually be in the reduced state while subunits A and C are in the oxidized state.

Low-Temperature Reduced Form. The structure of dithionite-reduced SOR was determined to ascertain whether changes to the overall structure and/or iron coordination occur upon iron reduction. As discussed above, in contrast to the different polypeptide conformations observed in the oxidized structures, the structure of SOR in the reduced form shows that the conformations of the Gly 9−Lys 15 and Gly 36−Pro 40 loop regions are the same in all four subunits. These regions in the SOR-RedLT structure share conformations very similar to the corresponding regions in subunits B and D of the SOR-OxRT structure, with the Cα rmsds between these regions of the two structures being 0.4 and 0.6 Å, respectively.

The iron centers of reduced SOR display the same pentacoordinate configuration in all four subunits. In subunits A and C, Glu 14 is no longer coordinated to the iron, as it was in the oxidized structure; in addition, the solvent molecule that was observed as a sixth ligand to the iron in subunits B and D of the SOR-OxLT model is no longer observed. While the iron center coordination is the same among the four subunits of SOR-RedLT, there are some notable differences between the sites in the apparent occupancies of the iron atom at each site. In both subunits B and D, the electron densities of the iron and two of the histidines to which it is coordinated (histidines 16 and 114) are considerably weaker than those in subunits A and C. Assuming that this reflects partial loss of iron, rather than high mobility, the occupancies of Fe in the B and D subunits were determined to be ∼0.2 through crystallographic refinement. Because of this low occupancy, the metal−ligand distances at these sites cannot be reliably determined, which likely contributes to the apparent changes in the values reported for SOR-RedLT subunits B and D in Table 3.

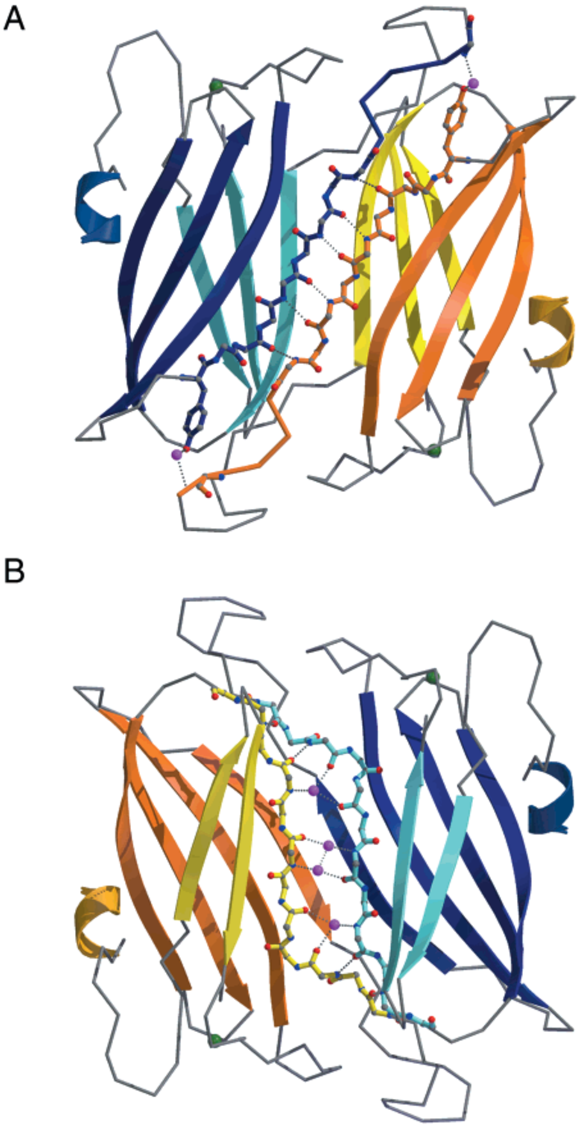

FIGURE 6: Dimerization interactions between subunits A (yellow) and C (blue) (the same interactions are observed for subunits B and D). As in Figure 3, lighter-colored β-strands correspond to the three-stranded β-sheet whereas darker-colored β-strands correspond to the four-stranded β-sheet. (A) View of subunits A and C showing hydrogen bonds formed between the D β-strands of the two subunits, resulting in the formation of an extended eight-stranded antiparallel β-sheet. (B) View upon rotation of the molecule by 180° about the vertical axis in the plane of the paper, showing the direct and water-mediated hydrogen bonds that are formed between the E β-strands of the two subunits.

Table 3: Bond Distances between the Iron Atom and Its Ligands (X) in the Different Subunits of the Oxidized (SOR-OxRT and SOR-OxLT) and Reduced (SOR-RedLT) Forms of SOR[a]

	SOR-OxRT		SOR-OxLT				SOR-RedLT			
X	A	B	A	B	C	D	A	B	C	D
His 16 Nϵ2	2.14	2.14	2.10	2.13	2.09	2.09	1.97	2.7	2.08	2.4
His 41 Nϵ2	2.15	2.21	2.17	2.21	2.20	2.24	2.29	2.7	2.26	3.1
His 47 Nϵ2	2.19	2.20	2.15	1.99	2.16	2.02	2.13	1.9	2.08	2.1
His 114 Nδ2	2.09	2.06	2.18	2.16	2.20	2.12	2.08	2.2	2.10	2.0
Cys 111 Sγ	2.42	2.33	2.46	2.68	2.46	2.67	2.44	2.6	2.40	2.7
Glu 14 Oϵ2	2.02	–	2.15	–	2.15	–	–	–	–	–
solvent	–	–	–	2.57	–	2.59	–	–	–	–

[a] The bond distances in subunits C and D of the SOR-OxRT model are not listed, as they are the same as those for subunits A and B, due to crystallographic symmetry. The bond distances reported for subunits B and D of the SOR-RedLT structure are less accurate due to the lower Fe occupancies at these sites and are therefore reported with lower precision values.

Mechanistic Implications. The fact that the sixth iron ligand is variable between the subunits of the oxidized structure as well as between the oxidized and reduced structures suggests that this variability could play a role in the catalytic mechanism of SOR. One possible role of having a variable sixth ligand may be to regulate the accessibility of superoxide to the iron site in the reduced and oxidized forms of SOR. According to eq 1a, superoxide should bind to SOR in the Fe(II) form. In the SOR-RedLT structure, the iron site is pentacoordinate, leaving the iron at the sixth ligand position exposed. One could speculate that superoxide may bind to the iron at this vacant sixth ligand position, forming a six-coordinate iron center; the superoxide would subsequently be reduced and released. In contrast, the iron centers in at least two of the subunits in the oxidized form of SOR are six-coordinate, with Glu 14 serving as the sixth ligand. In these subunits, the binding of superoxide to the iron would most likely be hindered, if not altogether prevented, by Glu 14. Such a gating mechanism could explain the binding of superoxide to the reduced, and not the oxidized, iron center.

It is not apparent from the structure, however, how binding of superoxide to the iron center is facilitated. In the case of both Cu,Zn SODs and also Mn and Fe SODs, it has been proposed that electrostatically positive residues around and along the substrate channel leading to the active site center serve to guide anions such as superoxide to the active site (*24*−*27*). This does not appear to be the case, however, for SOR. One difference between SOD and SOR is the apparent ease of accessibility of superoxide to the respective metal centers. In SOD, the active site is located at the bottom of a channel, whereas the iron center of SOR lies near the surface of the subunit. The seemingly more accessible active site of SOR may obviate the need for an electrostatic focusing effect such as that proposed for SOD. Lys 15, the positively charged residue closest to the iron center, could perhaps play some role in directing superoxide to the active site, but aside from this residue, the environment around the active site is mostly hydrophobic, as reflected by the surface electrostatic potential map calculated with GRASP (*21*) (Figure 8).

Upon substrate reduction, the Fe(III) center of SOR must be re-reduced to the Fe(II) form. As discussed in ref *1*, the likely electron donor for this electron-transfer reaction is the non-heme iron-containing protein rubredoxin (Rd). Since domain I of DFX contains an $FeCys_4$ rubredoxin-like center, the possibility that Rd is bound to SOR in a similar fashion as DFX domain I is attached to DFX domain II was explored. To test this possibility, one of the subunits of SOR was superimposed onto domain II of DFX while the structure of *P. furiosus* Rd (*5*) was superimposed onto domain I of DFX (rmsd of 1.3 Å among 21 Cα atoms). The superpositions revealed that *P. furiosus* Rd cannot bind to SOR in the same position and orientation in which domain I is attached to domain II of DFX, since this would result in *P. furiosus* Rd directly overlapping with another subunit of SOR.

Inspection of the SOR structure points instead to a potential Rd binding site involving the immediate solvent-exposed residues surrounding the iron center. Such residues

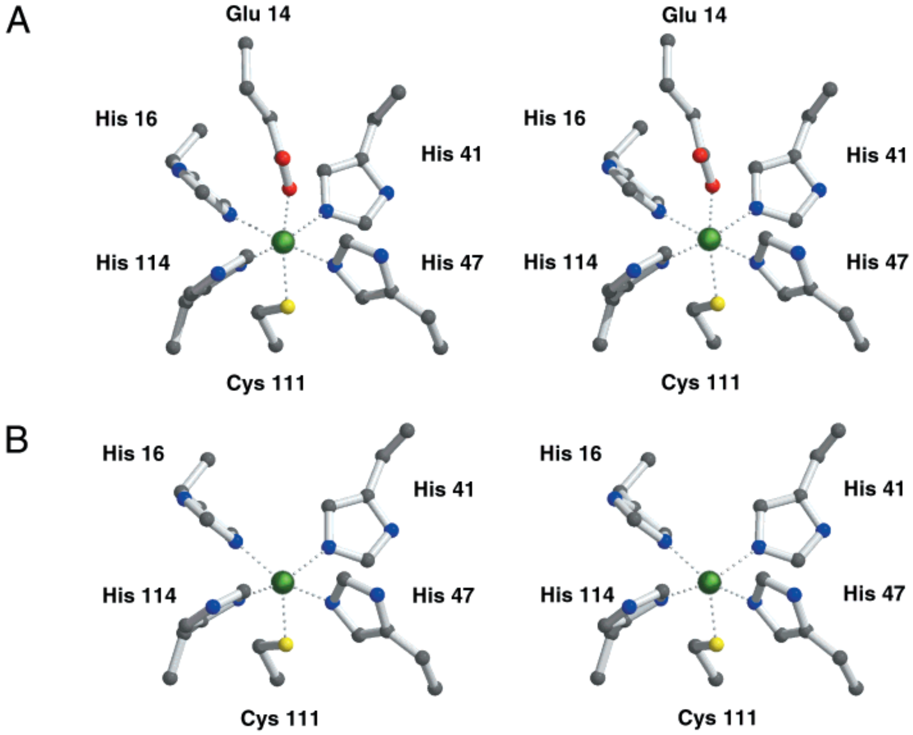

FIGURE 7: (A) Stereoview of the octahedral six-coordinate iron center observed in two (subunits A and C) of the four subunits of oxidized SOR. The iron, depicted as a green sphere, is coordinated in the equatorial positions by His 16, His 41, His 47, and His 114, and in the axial positions by Cys 111 and Glu 14. (B) Stereoview of the square pyramidal five-coordinate iron center observed in two (subunits B and D) of the four subunits of oxidized SOR as well as in all four subunits of reduced SOR. Glu 14 is no longer a ligand to the iron as a result of the Gly 9−Lys 15 loop region being in a different conformation in these subunits.

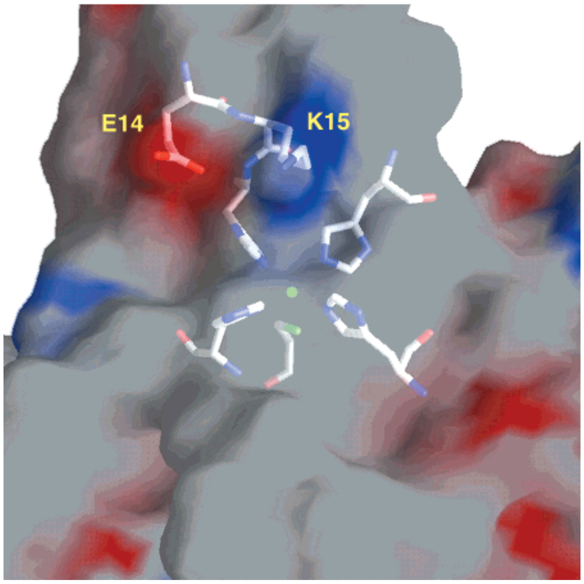

FIGURE 8: Electrostatic potential map contoured from $-15k_BT$ (red) to $+15k_BT$ (blue) showing the predominantly uncharged and relatively exposed environment of the iron center in reduced SOR. Glu 14 and Lys 15 are the charged residues closest to the iron, depicted as a green sphere. This figure was created using GRASP (*21*).

include three of the iron ligands, Glu 14, His 47, and His 114, as well as adjacent residues Trp 11, Ile 39, Pro 40, Pro 42, Thr 44, and Ile 113. One factor which suggests that Rd may bind at this site is the close proximity that can be achieved between the SOR and Rd iron centers if Rd were indeed to dock at this site. Compared to that at other potential binding sites, the binding of Rd at this position would result in the shortest iron-to-iron distance (∼8 Å), which perhaps would facilitate electron transfer between the two iron sites. In addition to the proximity between the iron centers, the hydrophobicity of the residues in this area provides another indication that Rd may bind at this location, since the structure of *P. furiosus* Rd (*5*, *6*) reveals that the majority of the solvent-exposed residues surrounding the $FeCys_4$ center in Rd are also hydrophobic. Finally, many of the above-mentioned residues surrounding the iron center in SOR are either a part of, or adjacent to, the flexible loop regions of Gly 9−Lys 15 and Gly 36−Pro 40. If these residues were indeed involved in binding Rd, the different conformations observed for the Gly 9−Lys 15 and Gly 36−Pro 40 regions between the oxidized and reduced structures could provide a mechanism by which Rd binding to SOR is regulated.

ACKNOWLEDGMENT

We greatly appreciate the contributions of Caroline Kisker, Hong Li, Hermann Schindelin, and Xiao-Dong Su to the structure determination.

REFERENCES

1. Jenney, F. E., Jr., Verhagen, M. F. J. M., Cui, X., and Adams, M. W. W. (1999) *Science 286*, 306−309.
2. Chen, L., Sharma, P., Le Gall, J., Mariano, A. M., Teixeira, M., and Xavier, A. V. (1994) *Eur. J. Biochem. 226*, 613−618.
3. Moura, I., Tavares, P., Moura, J. J. G., Ravi, N., Huynh, B.-H., Liu, M.-Y., and LeGall, J. (1990) *J. Biol. Chem. 265*, 21596−21602.
4. Coelho, A. V., Matias, P., Fülöp, V., Thompson, A., Gonzalez, A., and Carrondo, M. A. (1997) *J. Bioinorg. Chem. 2*, 680−689.

5. Day, M. W., Hsu, B. T., Joshua-Tor, L., Park, J.-B., Zhou, Z. H., Adams, M. W. W., and Rees, D. C. (1992) *Protein Sci. 1*, 1494−1507.
6. Bau, R., Rees, D. C., Kurtz, D. M., Scott, R. A., Huang, H. S., Adams, M. W. W., and Eidsness, M. K. (1998) *JBIC, J. Biol. Inorg. Chem. 3*, 484−493.
7. Jenney, F. E., Jr., Cui, X., Verhagen, M. F. J. M., and Adams, M. W. W. (2000) (manuscript in preparation).
8. Kabsch, W. (1988) *J. Appl. Crystallogr. 21*, 916−924.
9. Otwinowski, Z., and Minor, W. (1997) *Methods Enzymol. 276*, 307−326.
10. Soltis, S. M., Stowell, M. H. B., Wiener, M. C., Phillips, G. N., Jr., and Rees, D. C. (1997) *J. Appl. Crystallogr. 30*, 190−194.
11. Bailey, S. (1994) *Acta Crystallogr. D50*, 760−763.
12. Otwinowski, Z. (1991) in *CCP4 Study Weekend Isomorphous Replacement and Anomalous Scattering* (Wolf, W., Evans, P., and Leslie, A., Eds.) pp 80−86, SERC Daresbury Laboratory, Warrington, U.K.
13. Cowtan, K. (1994) *Joint CCP4 and ESF-EACBM Newsletter on Protein Crystallography 31*, 34−38.
14. Kleywegt, G. J., and Jones, T. A. (1996) *Acta Crystallogr. D52*, 826−828.
15. Brunger, A. T. (1992) *X-PLOR Manual Version 3.1: A System for X-ray Crystallography and NMR*, Yale University Press, New Haven, CT.
16. Read, R. J. (1986) *Acta Crystallogr. A42*, 140−149.
17. Jones, T. A., Zou, J. Y., Cowan, S. W., and Kjeldgaard, M. (1991) *Acta Crystallogr. A47*, 110−119.
18. Laskowski, R. A., MacArthur, M. W., Moss, D. S., and Thornton, J. M. (1993) *J. Appl. Crystallogr. 26*, 283−291.
19. Navaza, J. (1994) *Acta Crystallogr. A50*, 157−163.
20. Vaughn, D. E., and Bjorkman, P. J. (1996) *Neuron 16*, 261−273.
21. Nicholls, A., Sharp, K. A., and Honig, B. (1991) *Proteins 11*, 281−296.
22. Stroppolo, M. E., Nuzzo, S., Pesce, A., Rosano, C., Battistoni, A., Bolognesi, M., Mobilio, S., and Desideri, A. (1998) *Biochem. Biophys. Res. Commun. 249*, 579−582.
23. Ferraroni, M., Rypniewski, W., Wilson, K. S., Viezzoli, M. S., Banci, L., Bertini, I., and Mangani, S. (1999) *J. Mol. Biol. 288*, 413−426.
24. Getzoff, E. D., Tainer, J. A., Weiner, P. K., Kollman, P. A., Richardson, J. S., and Richardson, D. C. (1983) *Nature 306*, 287−290.
25. Klapper, I., Hagstrom, R., Fine, R., Sharp, K., and Honig, B. (1986) *Proteins: Struct., Funct., Genet. 1*, 47−59.
26. Sines, J., Allison, S., Wierzbicki, A., and McCammon, J. A. (1990) *J. Phys. Chem. 94*, 959−961.
27. Ludwig, M. L., Metzger, A. L., Pattridge, K. A., and Stallings, W. C. (1991) *J. Mol. Biol. 219*, 335−358.
28. Esnouf, R. M. (1997) *J. Mol. Graphics 15*, 133−138.
29. Merritt, E. A., and Bacon, D. J. (1997) *Methods Enzymol. 277*, 505−524.

BI992428K